

Identification of two-dimensional FeO₂ termination of hematite α -Fe₂O₃(0001) surface

*Jesús Redondo*¹, Petr Lazar³, Pavel Procházka⁴, Stanislav Průša⁴, Jan Lachnitt², Benjamín Mallada¹, Aleš Cahlík¹, Jan Berger¹, Břetislav Šmíd⁴, Pavel Jelínek¹, Jan Čechal*⁴, Martin Švec*¹*

1 - Institute of Physics, Czech Academy of Sciences, Prague, Czech Republic

2 - Faculty of Mathematics and Physics, Charles University, Prague, Czech Republic

3 - Regional Center for Advanced Materials and Technologies, Olomouc, Czech Republic

4 - Central European Institute of Technology, Brno, Czech Republic

ABSTRACT

Iron oxides are among the most abundant compounds on Earth and have consequently been studied and used extensively in industrial processes. Despite these efforts, concrete understanding of some of their surface phase structures has remained elusive, in particular the oxidized α -Fe₂O₃(0001) hematite surface. We detail an optimized recipe to produce this phase over the entire hematite surface and study the geometrical parameters and composition of its complex structure by means of atomically resolved microscopy, electron diffraction and surface-sensitive spectroscopies. We conclude that the oxidized α -Fe₂O₃(0001) surface is terminated by a two-dimensional iron oxide with structure, lattice parameters, and orientation different from the bulk substrate. Using total-energy density functional theory for simulation of a large-scale atomic model, we identify the structure of the surface layer as antiferromagnetic, conductive 1T-FeO₂ attached on half-metal terminated bulk. The model succeeds in reproducing the characteristic modulations observed in the atomically resolved images and electron diffraction patterns.

Mineral iron oxide is known to be available in many stoichiometries, polymorphs, and even mixtures. Hematite (α -Fe₂O₃), maghemite (γ -Fe₂O₃), magnetite (Fe₃O₄), and wüstite (Fe_{1-x}O) are prominent representatives of this class, possessing a wide range of electronic, magnetic and catalytic properties, due to their different oxygen content and characteristic crystal structures ¹. Currently, a significant amount of research is focused on the catalytic processes that occur on the surfaces of iron oxides, such as CO oxidation, wastewater purification, liquid fuel synthesis via Fischer-Tropsch reactions, styrene production or water splitting ².

The research on iron oxides has turned its focus to nanoparticles ³ and thin films, ⁴ which are economically advantageous and show versatility beyond that of bulk materials. The critical limit - 2D iron oxide films have been achieved in a form of a monolayer of FeO(111) on Pt(111) ⁵, Ag(111) ⁶, Ru(0001) ⁷ and Pd(111) ⁸. Nevertheless, stability of this monolayer is inherently linked to its strong hybridization with the metal substrate; it remains an open question whether it can exist independently or as termination of an iron oxide crystal ^{9,10}, in analogy with the recently revisited V₂O₃(0001) system ^{11,12}. Another recent survey on new possible candidates for 2D materials suggests that some trilayer structures of metal oxides (e.g. MnO₂, CoO₂, GeO₂) may be stable after exfoliation from a layered bulk ¹³.

The atomic structures of bulk Fe₃O₄ and α -Fe₂O₃ are well-known, but their surface terminations remain elusive ^{2,14}, owing to their complexity and the fact that their surface stoichiometry can be varied depending on the preparation. Specifically, by removing oxygen from the surface of α -Fe₂O₃(0001) by selective sputtering, a stoichiometry and structure resembling Fe₃O₄(111) can be attained ^{15,16}. Conversely, the surfaces can be partially or fully reoxidized by increasing the oxygen chemical potential (pressure) during annealing in ultra-high vacuum (UHV) ^{2,17}. The resulting reconstructions display a characteristic nanoscale pattern manifested as a floreted low-energy electron diffraction (LEED). It has been initially interpreted as an FeO(111) overlayer on top of the bulk ¹⁸, or later explained by coexistence of alternating domains of FeO(111) and α -Fe₂O₃(0001), based on images taken by scanning tunneling microscopy (STM). Thereafter the name "biphase" has been coined for this particular surface reconstruction ^{19,20}. Whereas several works use the biphase concept to explain microscopy and spectroscopy data ^{15,21-26}, other research somewhat counterintuitively suggests the existence of a thin Fe₃O₄(111) layer on the bulk,²⁷ or states that the surface is oxygen-terminated ²⁸. Moreover, despite a large number of density functional theory (DFT) calculations, currently there is no atomic model that comprehensively explains the various experimental observations ^{22,29-33}.

In this work, we prepare a single-phase, fully oxidized surface of α -Fe₂O₃(0001), with the objective of proposing a model of its atomic structure using a multitude of microscopy and spectroscopy techniques, and rationalize it by total-energy DFT.

Results and discussion

In order to prepare the reduced phase of the surface (R-phase), the sample was sputtered with Ar⁺ at 1 keV and subsequently annealed in UHV at 700 °C. Sputtering the surface selectively removes O atoms, which reduces the surface from Fe₂O₃ to stoichiometric Fe₃O₄^{15,34}. Long sputtering times are avoided as the reduction progresses into the bulk and its reoxidation poses a challenge³⁵. A complete coverage of the substrate with the R-phase can be readily achieved with a few (3-5) 10 minute sputtering cycles. This surface phase is relatively flat, with irregular-shaped terraces typically over 100 nm wide - as shown by the STM in Fig. 1a, along with its characteristic 2×2 micro-LEED (μLEED) pattern consisting of two rotational domains mutually offset by 60°, distinguishable by taking diffraction patterns of separate domains. These domains can be also resolved in real-space by low-energy electron microscopy (LEEM), using a composition of dark-field images (orange and blue, also shown in Fig. 1a) obtained by imaging only electrons diffracted to a direction associated with a particular domain orientation. These domains are equally represented on the surface.

Upon annealing for 30 min in 1×10⁻⁶ mbar of O₂ at 700 °C, the oxidized phase starts to grow (which we deliberately denote as *H-phase* for its characteristic honeycomb-like pattern, appearing in the STM shown in Fig. 2a). This level of re-oxidation is characterized by a heterogenous mixture of R- and H- phases, dominated by the R-phase; the STM reveals a morphologically complex landscape with a large number of small, atomically flat terraces with sizes typically around 50 nm (see Fig. 1b).

The final stage of the R- to H-phase transformation is accompanied by the growth of large single-domain terraces that often span over several hundreds of nm, typically divided by bunches of steps. It takes several hours of annealing in O₂ to fully transform the remaining R-phase into the H-phase, as indicated by complete disappearance of the 2×2 fractional spots in the diffraction pattern shown in Fig. 1c. The need for long annealing times well above 1h in O₂ to fully reoxidize the surface was already addressed by Saunders *et al.*, who observed that a single 30 min annealing at 700 °C led to no significant changes, on the other hand a significantly longer (90 min) annealing completely reoxidized the surface³⁴. It has also been observed that the recovery of the Fe₂O₃ stoichiometry in the surface and subsurface region requires achieving the correct temperature³⁵.

In the course of the transition from the R- to the H-phase, the X-ray photoelectron spectroscopy (XPS) Fe 2*p* lineshape undergoes a characteristic evolution³⁶. The appearance of satellite peaks at 732.8 and 719.0 eV indicates the development of the Fe³⁺ oxidation state

(XPS spectra in Fig. 1b,c). However, using these spectra to quantify the progress of the transformation is problematic (or the Fe oxidation/spin state), mostly due to its notoriously complicated multiplet splitting³⁷.

Once the H-phase is formed, sample annealing in vacuum up to 900 °C does not cause any reversal to the R-phase detectable by our methods. The surface covered by H-phase remains unaltered in UHV for several days; even after exposing it to air it is partially recoverable by in-vacuum annealing. In the latter case, we observed that a fraction of R-phase is formed upon re-insertion into UHV and annealing, which can be attributed to the effect of adventitious C being trapped from the atmosphere^{38,39} (more details about the effect of air exposure and annealing in vacuum can be found in Fig. S1).

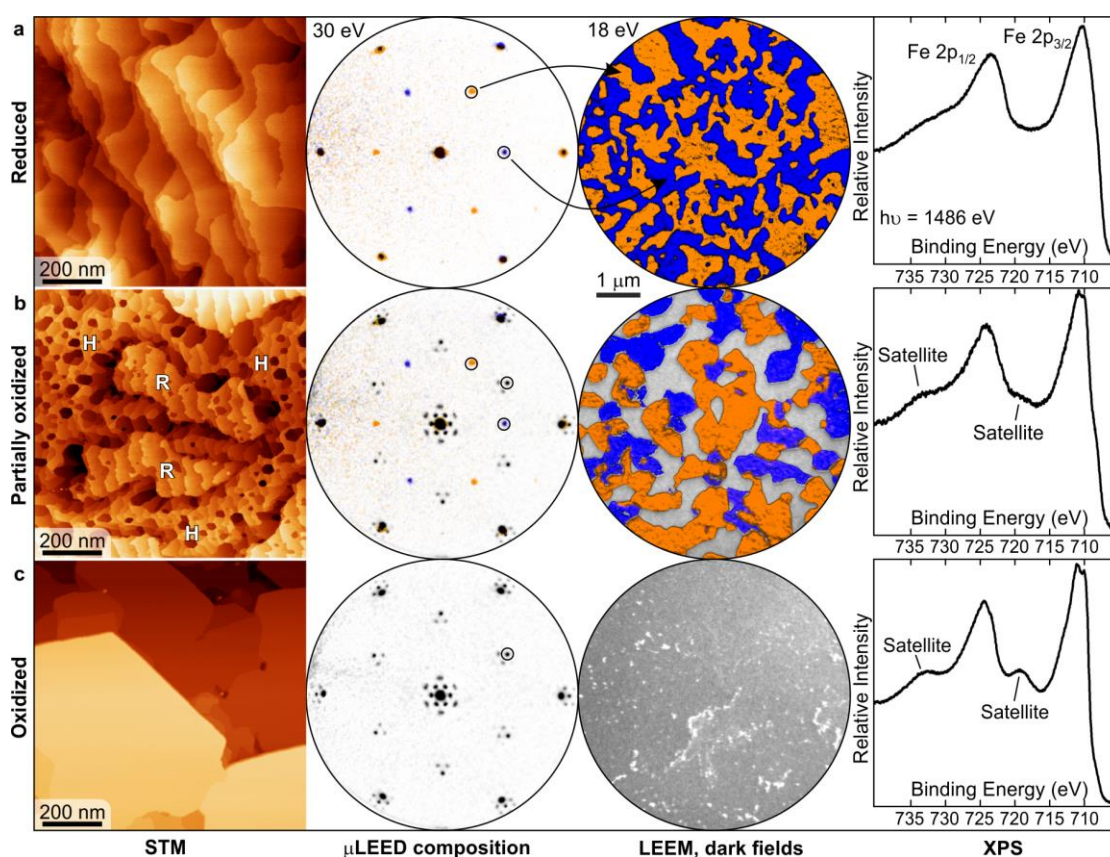


Figure 1: Oxidation process of the $\alpha\text{-Fe}_2\text{O}_3(0001)$ surface monitored by STM, μLEED , LEEM, and XPS (from left to right). a) Stoichiometric $\text{Fe}_3\text{O}_4(111)$ surface obtained after sputtering and annealing in UHV. Colored μLEED and dark-field LEEM images reveal two rotational domains (shown in orange and blue). b) Partially oxidized surface after initial 30 min. annealing in O_2 . Satellite peaks in the Fe $2p$ XPS corresponding to Fe^{3+} begin to develop. c) Completely oxidized surface featuring large terraces.

Figure 2a shows a representative STM image of a smaller area of the H-phase surface displaying a superstructure on two terraces divided by a step edge ($\Delta z = 0.48 \pm 0.02 \text{ nm}$). The superstructure visible on both terraces is hexagonal, resembling a honeycomb. The orientation of the higher and lower terrace honeycombs differs by an angle of $8 \pm 1^\circ$. The average periodicity is $40 \pm 1 \text{ \AA}$. The spatial frequency and the angle of the mutual domain rotation can be corroborated by comparing the combined FFT power spectrum in Fig. 2b, derived from the STM image, with colors distinguishing the rotational domains, a μLEED pattern taken near the (00) spot (Fig. 2c), also combined from two single domain diffraction patterns taken on two rotational domains. These reciprocal space images are in good agreement, with the periodicity and the angle being reproduced.

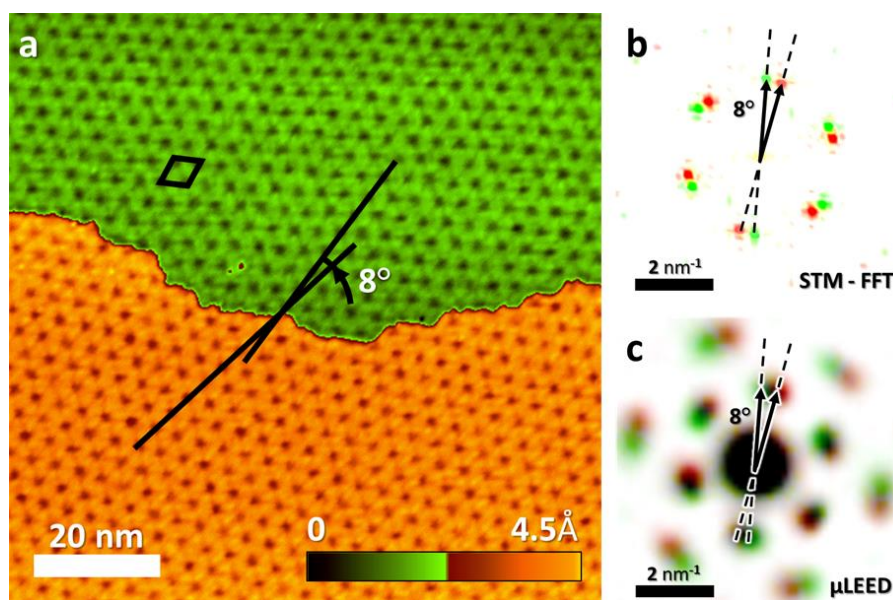


Figure 2: Characterization of the honeycomb superstructure. a) STM constant-current image, setpoint 0.3 nA, 1.4 V. The black lines mark the apparent domain orientations. b) FFT image combined from the upper terrace (green) and lower terrace (orange). c) μLEED of the (00) spot area, colored and composed from the patterns acquired from two adjacent terraces observed in LEEM, measured with 30 eV electron energy and 185 nm electron beam spot diameter. The dashed black lines denote the honeycomb domain orientations; the black arrows are their corresponding reciprocal supercell vectors.

The two atomically-resolved STM images in Figs. 3a,b show in detail a few supercells of the honeycomb superstructure. We would like to emphasize that the only difference between these two very distinct contrast types is the tip state; both types of contrast were regularly observed on the identical surface phase, and are independent of the bias voltage. Figure 3a shows a uniform layer with a periodicity of $3.08 \pm 0.08 \text{ \AA}$, intensity-modulated by the 40 \AA

honeycomb strikingly reminiscent of a moiré pattern. Figure 3b shows the same long-range modulation, but due to an emerging local $\sqrt{3}\times\sqrt{3}$ periodicity. The latter type of contrast corresponds to previous works^{19,20}; however our measurement provides higher resolution and proves that there are extra bright spots in the regions with the $\sqrt{3}\times\sqrt{3}$ periodicity that are all within the same first 1×1 sublattice.

Figure 3c shows the LEED pattern associated with this surface, exhibiting the characteristic florets around the bulk diffraction spots^{18,19}. The (01) and (11) spots originate from the bulk α - $\text{Fe}_2\text{O}_3(0001)$ ⁴⁰ unit cell and are taken as the reference ($a_{\text{bulk}} = 5.038 \text{ \AA}$)⁴¹ for the purpose of the superstructure analysis. The apparent angle of the superstructure orientation (denoted by a black vector on a dashed line in Fig. 3c with respect to the (10) bulk vector is $|\alpha| = 26^\circ \pm 0.5^\circ$. Notably, the most intense spots (marked by a cyan vector) are located within the florets around the (11) bulk spots. Their shape is tangentially elongated, since they comprise two individual spots. We determined the corresponding periodicity to be $a_{\text{top}} = 3.14 \pm 0.01 \text{ \AA}$, which reasonably matches the fine modulation observed via STM and its rotation with respect to the (11) vectors as $\delta = 0.31^\circ \pm 0.04^\circ$.

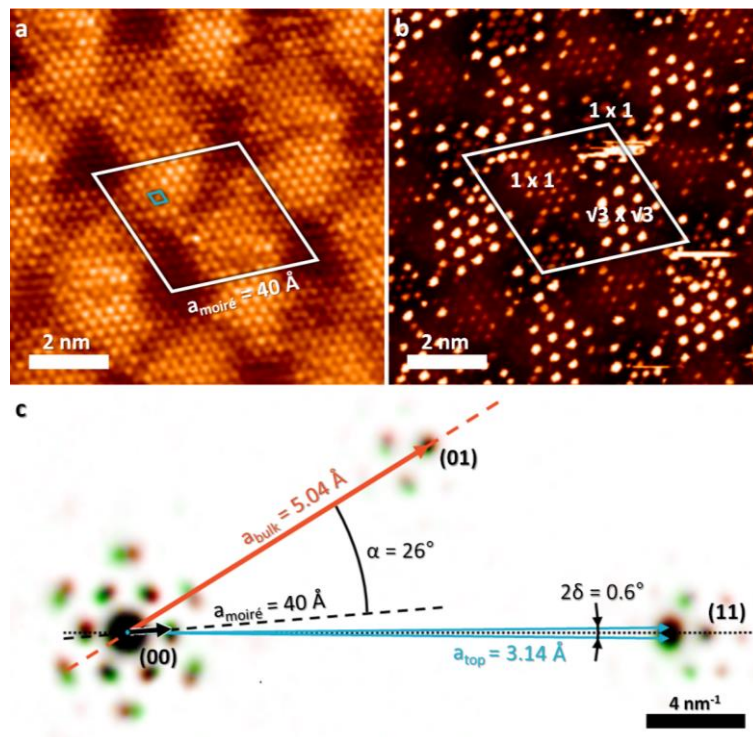


Fig. 3: STM and LEED analysis of the surface superstructure. a,b) Atomically resolved STM constant-height images of the H-phase obtained with two different contrasts at 0.2 V and 0.6 V, average currents 2.6 nA and 4.5 nA, respectively. The white rhombus tentatively marks the superstructure unit cell. c) Detail of the LEED pattern, composed of two images (red and green), taken on adjacent domains at 30 eV with 185 nm electron beam spot diameter. The

orange and cyan vectors mark the periodicities corresponding to the bulk α -Fe₂O₃(0001) and top layer, respectively. The black vector and the dashed line mark the periodicity and orientation of one moiré domain.

The overall character of the LEED pattern and the contrast in the STM images is consistent with a moiré arising from the coincidence of two unequal lattices; given the well-defined bulk properties, this can only be explained by the existence of an Fe oxide layer with specific lattice constant and atomic structure, different from its carrier - the α -Fe₂O₃(0001) bulk crystal.

However, the composition of the top layer and exact atomic arrangement remains ambiguous. To address this ambiguity we have performed low-energy ion scattering (LEIS) experiments employing He⁺ ions with energies of 1.4 - 5.0 keV. LEIS is primarily sensitive to composition of the topmost atomic layer making it particularly useful to determine the surface termination. The scattering spectra measured on the H-phase given in Fig. S2 show the presence of both Fe and O species on the surface (a comprehensive description of the measurements and quantification is given in the SI). From the peak intensities and energy dependence we have determined the Fe and O atom concentrations as $0.5 \times 10^{15} \text{ cm}^{-2}$ and $1.7 \times 10^{15} \text{ cm}^{-2}$, respectively, which indicates prevalence of oxygen in the topmost layer and in the near surface region accessible by LEIS.

The abundance of oxygen in the terminal layers narrows the choice of possible models explaining the surface termination. We design previously unexplored models that can potentially be self-supporting and not disrupted by the substrate. Promising candidates are layered structures analogous to transition metal dichalcogenides, in which a hexagonal lattice of Fe atoms is sandwiched between two hexagonal O layers. Two most common structures of transition metal dichalcogenides are a hexagonal 2H phase (space group, P6₃/mmc) and a trigonal 1T phase (space group, P $\bar{3}$ m1), shown in Fig. S4. To the best of our knowledge, such structures of an iron oxide have been neither proposed nor observed so far. Therefore, we employ first-principles DFT calculations to elucidate the basic properties of this form of iron oxide. The calculated phonon spectra of the single-layer free-standing 2H-FeO₂ and 1T-FeO₂ (Fig. S5) show that both structures are dynamically stable, i.e. there are no imaginary frequencies which would indicate a spontaneous collapse. The total energy of the 1T phase is lower by 0.88 eV per formula unit than that of the 2H, thus the 1T phase is thermodynamically far more stable (for details about how the calculations were carried out and the stability of the models please see SI).

Having established through simulation that 1T-FeO₂ is stable and thermodynamically favourable, we investigate its magnetic and electronic properties by evaluating the energy of several possible magnetic states of this structure: high-spin ferromagnetic configuration, low-spin ferromagnetic (FM), and antiferromagnetic (AFM) alignment of spins. The spin moments in each configuration reside on Fe atoms, while the projected spin moments on O atoms are negligible. The most stable configuration turns out to be AFM; the energy of the high spin FM ordering is 0.14 eV per formula unit higher. The low spin FM is an additional 0.97 eV higher than the FM value. The projected spin moments are $\pm 3.79 \mu_B$ in the AFM configuration. The spin moments are parallel in one of the in-plane directions and antiparallel in the second. The lattice parameter of the free standing 1T-FeO₂ is 2.97 Å in the AFM state and 2.98 Å in the high-spin FM state. The projection of the density of states reveals that the free-standing 1T-FeO₂ is metallic (Fig. S6) in all spin configurations. For the supported 1T-FeO₂, the coupling to underlying hematite support can influence the position of its Fermi level and hence the layer conductivity and spin configuration.

Finally, we shall address how the layer is bonded to the hematite bulk. Its structure consists of separate hexagonal Fe and O₃ layers stacked as a sequence of Fe-O₃-Fe units along the [0001] direction, meaning that the unreconstructed (0001) surface of hematite has three possible terminations. Earlier DFT calculations suggested that the Fe termination containing half of the inter-plane Fe, termed a “half-metal” termination, should be stable at low oxygen pressures⁴². According to the same work the O₃-termination becomes stabilized at high oxygen pressure by a substantial relaxation of the surface atoms.

Two full supercell models were used, made of $\begin{smallmatrix} 13 & 1 \\ -1 & 12 \end{smallmatrix}$ 1T-FeO₂ relaxed on $\begin{smallmatrix} 9 & 5 \\ -5 & 4 \end{smallmatrix}$ Fe- and O₃-terminated α -Fe₂O₃(0001), which matched best with the geometrical parameters of the real system (details about the geometrical derivation of the model from experimental data can be found in the SI and Fig. S7. Corresponding profiles of the atomic models are shown in Fig. 4b and S8, respectively). The resulting calculated formation energies, displayed in Fig. S9, demonstrate that the model of the 1T-FeO₂ on the Fe-terminated hematite is more stable than O₃-terminated hematite under any reasonable chemical potential of oxygen. The stability is due to stronger bonding of 1T-FeO₂ to the support. The estimation of the binding energy (energy needed to cleave the FeO₂ layer from the support) is 1.07 J/m² for the model on Fe-terminated bulk, whereas it amounts to just 0.12 J/m² for the O₃-terminated support, a value typical for noncovalent van der Waals bonding.

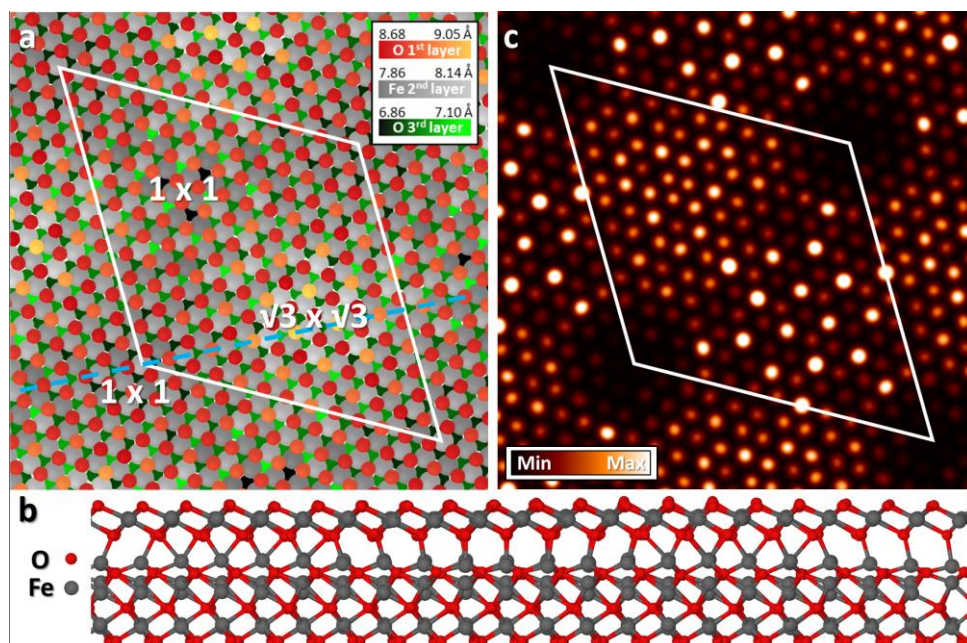


Fig. 4: Evaluation of the 1T-FeO₂ on α-Fe₂O₃(0001) relaxed model. a) the scheme of atomic heights in the three topmost surface layers (O 1st, Fe 2nd and O 3rd layers, with the unit cell marked by a white rhombus, and local reconstructions labelled, b) ball-and-stick profile of the structure. The plane of projection is denoted by the blue dashed line in a). c) simulation of a constant-height STM image.

The interface Fe atom coordination geometry varies gradually throughout the supercell between tetra- and octahedral, due to the lattice mismatch with the O atoms in the 3rd layer, and leads to a relaxation of the O and Fe atoms in the entire FeO₂ layer in directions both parallel and vertical with respect to the surface. Moiré modulation and local $\sqrt{3}\times\sqrt{3}$ periodicity arise within the FeO₂ layer, as a consequence of the height variation of the topmost O atoms (1st layer), as depicted by the model in Fig. 4a, color coded according to separate layers and individual atom heights. This phenomenon effectively splits the supercell into three dissimilar regions, of which one has $\sqrt{3}\times\sqrt{3}$ and two retain the original 1×1 periodicity. The height variation of the O atoms in the 1st layer directly translates into the contrast variation obtained by a constant-height STM simulation, in Fig. 4c, made with the Tersoff-Hamann approximation, at a distance of 0.25 nm from the surface plane, tunneling in the range -0.5 eV to 0 eV. The resulting image yields the contrast and characteristic features consistent with both the original^{19,20} and present STM observations. The projection of spin moments indicates a local rearrangement of the Fe electrons within the 1×1 regions; the projected spin values for Fe atoms vary locally between 2.6 and 4.2 μB in the dark 1×1 area and between 3.3 to 4.4 μB in the brighter 1×1 area. In the $\sqrt{3}\times\sqrt{3}$ regions, the spin is distributed more evenly - between 3.6 and 4.3 μB.

Conclusions

We conclude from our experimental evidence, well supported by fully relaxed large scale calculations, that the surface termination of α -Fe₂O₃(0001) takes the form of a continuous two-dimensional 1T-FeO₂ layer attached to the half-metal termination of the bulk crystal. The proposed model matches the available experimental evidence and resolves the long-standing controversy about the termination of the α -Fe₂O₃(0001) surface. According to the theoretical calculations, the 2D layer of 1T-FeO₂ possesses interesting material properties, a metallic character with antiferromagnetic spin arrangement, highly appealing for spintronic applications. We anticipate that these findings can stimulate new research in the field of 2D oxide materials.

References

1. Cornell, R. M. & Schwertmann, U. *The Iron Oxides: Structure, Properties, Reactions, Occurrences and Uses*. (John Wiley & Sons, 2006).
2. Parkinson, G. S. Iron oxide surfaces. *Surf. Sci. Rep.* **71**, 272–365 (2016).
3. Mohammed, M. *et al.* Iron Oxide Nanoparticles. in *Nanomaterials* (2011).
4. Weiss, W. & Ranke, W. Surface chemistry and catalysis on well-defined epitaxial iron-oxide layers. *Prog. Surf. Sci.* **70**, 1–151 (2002).
5. Ritter, M., Ranke, W. & Weiss, W. Growth and structure of ultrathin FeO films on Pt(111) studied by STM and LEED. *Phys. Rev. B: Condens. Matter Mater. Phys.* **57**, 7240–7251 (1998).
6. Waddill, G. D. & Ozturk, O. Epitaxial growth of iron oxide films on Ag(111). *Surf. Sci.* **575**, 35–50 (2005).
7. Ketteler, G. & Ranke, W. Self-assembled periodic Fe₃O₄ nanostructures in ultrathin FeO(111) films on Ru(0001). *Phys. Rev. B: Condens. Matter Mater. Phys.* **66**, (2002).
8. Zeuthen, H. *et al.* Structure of Stoichiometric and Oxygen-Rich Ultrathin FeO(111) Films Grown on Pd(111). *J. Phys. Chem. C* **117**, 15155–15163 (2013).
9. Netzer, F. P. & Fortunelli, A. *Oxide Materials at the Two-Dimensional Limit*. (Springer, 2016).
10. Obermüller, T., Doudin, N., Kuhness, D., Surnev, S. & Netzer, F. P. Ultrathin oxide films: Epitaxy at the two-dimensional limit. *J. Mater. Res.* **32**, 3924–3935 (2017).
11. Window, A. J. *et al.* V₂O₃(0001) surface termination: phase equilibrium. *Phys. Rev. Lett.* **107**, 016105 (2011).

12. Feiten, F. E. *et al.* Surface structure of $V_2O_3(0001)$ revisited. *Phys. Rev. Lett.* **114**, 216101 (2015).
13. Ashton, M., Paul, J., Sinnott, S. B. & Hennig, R. G. Topology-Scaling Identification of Layered Solids and Stable Exfoliated 2D Materials. *Phys. Rev. Lett.* **118**, 106101 (2017).
14. Kuhlenbeck, H., Shaikhutdinov, S. & Freund, H.-J. Well-ordered transition metal oxide layers in model catalysis--a series of case studies. *Chem. Rev.* **113**, 3986–4034 (2013).
15. Tang, Y., Qin, H., Wu, K., Guo, Q. & Guo, J. The reduction and oxidation of $Fe_2O_3(0001)$ surface investigated by scanning tunneling microscopy. *Surf. Sci.* **609**, 67–72 (2013).
16. Genuzio, F., Sala, A., Schmidt, T., Menzel, D. & Freund, H.-J. Interconversion of α - Fe_2O_3 and Fe_3O_4 Thin Films: Mechanisms, Morphology, and Evidence for Unexpected Substrate Participation. *J. Phys. Chem. C* **118**, 29068–29076 (2014).
17. Diebold, U., Li, S.-C. & Schmid, M. Oxide surface science. *Annu. Rev. Phys. Chem.* **61**, 129–148 (2010).
18. Kurtz, R. L. & Henrich, V. E. Geometric structure of the α - $Fe_2O_3(001)$ surface: A leed and XPS study. *Surface Science Letters* **129**, A243 (1983).
19. Condon, N. G. *et al.* Biphase Ordering of Iron Oxide Surfaces. *Phys. Rev. Lett.* **75**, 1961–1964 (1995).
20. Condon, N. G. *et al.* Biphase ordering on $Fe_3O_4(111)$. *Phys. Rev. B: Condens. Matter Mater. Phys.* **55**, 15885–15894 (1997).
21. Ketteler, G., Weiss, W., Ranke, W. & Schlögl, R. Bulk and surface phases of iron oxides in an oxygen and water atmosphere at low pressure. *Phys. Chem. Chem. Phys.* **3**, 1114–1122 (2001).
22. Lewandowski, M. *et al.* Nanoscale Patterns on Polar Oxide Surfaces. *Chem. Mater.* **28**, 7433–7443 (2016).
23. Shaikhutdinov, S. K. & Weiss, W. Oxygen pressure dependence of the α - $Fe_2O_3(0001)$ surface structure. *Surf. Sci.* **432**, L627–L634 (1999).
24. Camillone, N., III *et al.* Surface termination dependence of the reactivity of single crystal hematite with CCl_4 . *Surf. Sci.* **511**, 267–282 (2002).
25. Herman, G. S., McDaniel, E. P. & Joyce, S. A. Interaction of D_2O with the $Fe_3O_4(111)$ and the biphase ordered structures on α - $Fe_2O_3(0001)$. *J. Electron Spectrosc. Relat. Phenom.* **101-103**, 433–438 (1999).

26. Huang, W., Ranke, W. & Schlögl, R. Reduction of an α -Fe₂O₃(0001) Film Using Atomic Hydrogen. *J. Phys. Chem. C* **111**, 2198–2204 (2007).
27. Lanier, C. H., Chiaramonti, A. N., Marks, L. D. & Poepplmeier, K. R. The Fe₃O₄ origin of the 'Biphase' reconstruction on α -Fe₂O₃(0001). *Surf. Sci.* **603**, 2574–2579 (2009).
28. Berdunov, N., Murphy, S., Mariotto, G. & Shvets, I. V. Room temperature study of a strain-induced electronic superstructure on a magnetite (111) surface. *Phys. Rev. B Condens. Matter* **70**, 10 (2004).
29. Rohrbach, A., Hafner, J. & Kresse, G. Ab initio study of the (0001) surfaces of hematite and chromia: Influence of strong electronic correlations. *Phys. Rev. B: Condens. Matter Mater. Phys.* **70**, (2004).
30. Bergermayer, W., Schweiger, H. & Wimmer, E. Ab initio thermodynamics of oxide surfaces: O₂ on Fe₂O₃(0001). *Phys. Rev. B Condens. Matter* **69**, B864 (2004).
31. Kiejna, A. & Pabisiak, T. Mixed Termination of Hematite α -Fe₂O₃(0001) Surface. *J. Phys. Chem. C* **117**, 24339–24344 (2013).
32. Huang, X., Ramadugu, S. K. & Mason, S. E. Surface-Specific DFT + U Approach Applied to α -Fe₂O₃(0001). *J. Phys. Chem. C* **120**, 4919–4930 (2016).
33. Ketteler, G., Weiss, W. & Ranke, W. Surface structures of α -Fe₂O₃(0001) phases determined by LEED crystallography. *Surf. Rev. Lett.* **08**, 661–683 (2001).
34. Pollak, M. *et al.* An in-situ study of the surface phase transitions of α -Fe₂O₃ by X-ray absorption spectroscopy at the oxygen K-edge. *Nucl. Instrum. Methods Phys. Res. B* **97**, 383–386 (1995).
35. Kim, C.-Y., Escudro, A. A., Bedzyk, M. J., Liu, L. & Stair, P. C. X-ray scattering study of the stoichiometric recovery of the α -Fe₂O₃(0001) surface. *Surf. Sci.* **572**, 239–246 (2004).
36. McIntyre, N. S. & Zetaruk, D. G. X-ray photoelectron spectroscopic studies of iron oxides. *Anal. Chem.* **49**, 1521–1529 (1977).
37. Grosvenor, A. P., Kobe, B. A., Biesinger, M. C. & McIntyre, N. S. Investigation of multiplet splitting of Fe 2p XPS spectra and bonding in iron compounds. *Surf. Interface Anal.* **36**, 1564–1574 (2004).
38. Barr, T. L. & Seal, S. Nature of the use of adventitious carbon as a binding energy standard. *J. Vac. Sci. Technol. A* **13**, 1239–1246 (1995).

39. Miller, D. J., Biesinger, M. C. & McIntyre, N. S. Interactions of CO₂ and CO at fractional atmosphere pressures with iron and iron oxide surfaces: one possible mechanism for surface contamination? *Surf. Interface Anal.* **33**, 299–305 (2002).
40. Lad, R. J. & Henrich, V. E. Structure of α -Fe₂O₃ single crystal surfaces following Ar⁺ ion bombardment and annealing in O₂. *Surf. Sci.* **193**, 81–93 (1988).
41. Gualtieri, A. F. & Venturelli, P. In situ study of the goethite-hematite phase transformation by real time synchrotron powder diffraction. *Am. Mineral.* **84**, 895–904 (1999).
42. Wang, X.-G. *et al.* The Hematite α -Fe₂O₃(0001) Surface: Evidence for Domains of Distinct Chemistry. *Phys. Rev. Lett.* **81**, 1038–1041 (1998).

Acknowledgements

We would like to thank to Prof. H. J. Freund (Fritz-Haber Institute, Berlin), Dr. Jaeyoung Kim (PAL, Pohang, Korea) for fruitful discussions and support and Lukáš Kormoš for assistance with sample preparation. The research was supported by the Ministry of Education, Youth and Sports of the Czech Republic LQ1601 (CEITEC 2020). Part of the work was carried out with the support of CEITEC Nano Research Infrastructure (MEYS CR, 2016–2019). The authors also acknowledge the CERIC-ERIC Consortium for the access to experimental facilities. The authors are grateful to Jack Hellerstedt for assistance in writing of the manuscript.

Author Contributions

J.R. performed the main STM measurements. P.P. and J.Č. realized the LEEM experiments. A.C. and B.M. developed the preparation procedure. S.P. carried out the LEIS measurements and data analysis. B.Š. carried out the XPS measurements. J.B. assisted in preparation of the samples. P.L. performed the theoretical calculations, J.L. assisted in the creation of the geometrical model. M.Š. and J.R. evaluated the experimental data and wrote the paper. M.Š. and P.J. proposed and initiated the experiments and calculations. All the authors reviewed and discussed the manuscript thoroughly before submission.

Methods

Natural α -Fe₂O₃(0001) single crystal samples were acquired from SurfaceNet GmbH and mounted on Mo/Ta plates for STM, LEED and XPS measurements. STM and LEED characterization was carried out at room temperature in a UHV VT-STM (Scienta Omicron GmbH), XPS spectra were recorded at the NAP-XPS (Specs GmbH) of the Faculty of Mathematics and Physics of the Charles University. The temperature was monitored by a Micro-Epsilon ® 2MH - CF3 thermoMETER of 1.6 μ m spectral range focused on the center of the sample, measuring in the range of 385-1600 °C with a spectral emissivity of 0.6. Electrochemically etched W tips were used for scanning. LEEM/ μ LEED and LEIS measurements were performed with a FE-LEEM P90 (Specs GmbH) instrument and a Qtac 100 (Ion TOF GmbH), respectively. Here the samples were prepared in a separate UHV chamber and moved to the instruments for analysis via a linear transfer system without breaking the UHV conditions; the base pressure in all chambers was below 2×10^{-10} mbar. In the preparation done for LEEM and LEIS, the sample temperature was calibrated by a K-type thermocouple and checked by the pyrometer.

Data Availability

The data that support the findings of this study are available from the corresponding authors upon reasonable request.

Identification of two-dimensional FeO₂ termination of hematite α -Fe₂O₃(0001) surface - Supporting Information

Jesús Redondo^{1,2}, Petr Lazar³, Pavel Procházka⁴, Stanislav Průša⁴, Jan Lachnitt²,
Benjamín Mallada¹, Aleš Cahlík¹, Jan Berger¹, Břetislav Šmíd⁴, Pavel Jelínek¹, Jan
Čechal*⁴, Martin Švec*¹*

1 - Institute of Physics, Czech Academy of Sciences, Prague, Czech Republic

2 - Faculty of Mathematics and Physics, Charles University, Prague, Czech Republic

3 - Regional Center for Advanced Materials and Technologies, Olomouc, Czech Republic

4 - Central European Institute of Technology, Brno, Czech Republic

Effect of air exposure and annealing in vacuum

All the α -Fe₂O₃(0001) samples were mechanically cut and polished from natural hematite crystals. The characteristic LEED pattern of a mixture of R- and H- phases is obtained upon degassing as received samples in UHV at 700 °C, and the surface is clean enough to achieve atomic resolution in STM.

In order to study the effects of air exposure on the H- phase, we prepared sample completely covered with the H-phase. A blurry LEED pattern is observed after 30 min air exposure. Annealing of the air-exposed H- phase leads to a partial transformation of the H-phase to the R-phase, as evidenced in Fig. S1a. STM image indicates that ~ 30% of the H-phase is reduced.

XPS measurements carried out after air exposure before annealing reveal the presence of adventitious carbon on the surface, as shown in blue in Fig S1b. The four main sources of carbon contamination of surfaces exposed to air and UHV are graphite, hydrocarbons, CO and CO₂. In the case of iron and iron oxides surfaces, it has been proposed that the source of carbon is mainly CO and CO₂, which are fixed to the surface and form a thicker layer on the surface the longer the exposition time¹. For this reason, we relate the partial decomposition of the H-phase to the reaction with the adsorbed C species.

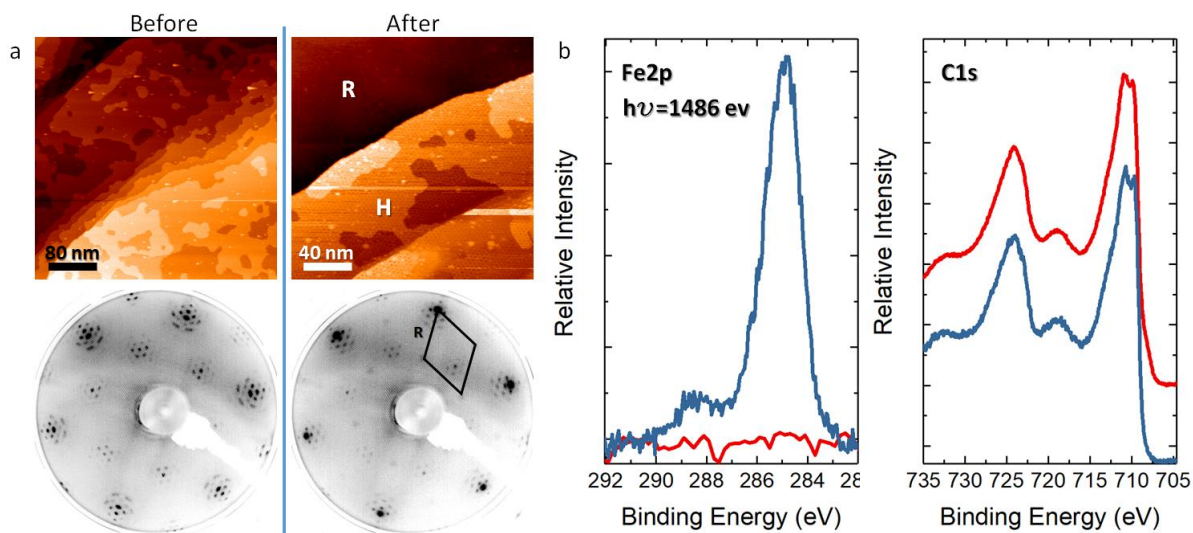


Fig.S1: Comparison of the $\alpha\text{-Fe}_2\text{O}_3(0001)$ before and after exposure to ambient air conditions. a) STM and LEED characterization of the surface. A portion of the H-phase transforms upon annealing. b) XPS spectra of the C1s and Fe 2p peaks before (red) and after (blue) air exposure (without annealing).

Finally, we investigated the results of annealing both pure R- and H-phases up to 900 °C for 18 hours in UHV (1×10^{-9} mbar). Based on LEED and STM measurements, we conclude that the surface structures and total coverages of the R- and H-phase remain unaltered, contrary to the transformations from H- to R- phase and vice versa observed on thin $\alpha\text{-Fe}_2\text{O}_3(0001)$ films grown metals ².

Low-energy ion scattering experiments

The LEIS technique is known for its extreme surface sensitivity³. The elemental composition of the top-most atomic layer is reflected by the presence of surface peaks of individual elements in the measured energy spectrum. The signal intensity (surface peak area) is proportional to the surface atomic concentration of the respective element n_i ⁴:

$$S_i = n_i \frac{d\sigma_i}{d\Omega} c P_i^+.$$

Here the measured signal is normalized to the unit primary beam charge of 1 nC (see the vertical scale unit in Fig. S2).

The differential scattering cross section $d\sigma/d\Omega$ is followed by the instrumental factor c , and P^+ is the ion fraction representing the probability that the projectile leaves the surface in the charged state. The ion fraction P^+ is expressed in the form of an exponential function, in which v_c is the characteristic velocity of the projectile–target atom pair³:

$$P^+ = \exp\left(v_c \frac{1}{v}\right).$$

$\frac{1}{v}$ expresses the sum of $\frac{1}{v_i}$ and $\frac{1}{v_f}$, where v_i and v_f are the limit velocities of the projectile at incoming and outgoing trajectories. The particular definition of the inverse velocities depends on the actual combination of the charge exchange processes involved in the collision.

The theoretical prediction of P^+ is difficult. The ion fraction is influenced by many charge exchange processes between the projectile and the surface under analysis. Each neutralization mechanism is dominant at a specific distance between the projectile and the target surface or an individual target atom. We will focus on two charge exchange processes that are relevant to our analysis; the Auger neutralization (AN) and the collision induced neutralization (CIN). While AN is effective when the projectile and target atom orbitals overlap, CIN dominates during the closest approach of the colliding partners. Thus, AN defines the inverse velocity at lower primary energies, and CIN take over at the higher primary energies.

Figure S2 contains four spectra measured under identical experimental conditions (helium primary beam with kinetic energy 3.0 keV and scattering angle 145°). The red spectrum represents the signal measured on the H-phase of $\alpha\text{-Fe}_2\text{O}_3(0001)$; it features an Fe surface peak at 2310 eV and an O peak at 1180 eV. The green and black spectra were measured on polycrystalline Cu and Fe references cleaned by Ar sputtering (fluence 3×10^{16} ions/cm²). The blue spectrum was measured on a SiO₂ surface cleaned by Ne sputtering (fluence 1×10^{16} ions/cm²).

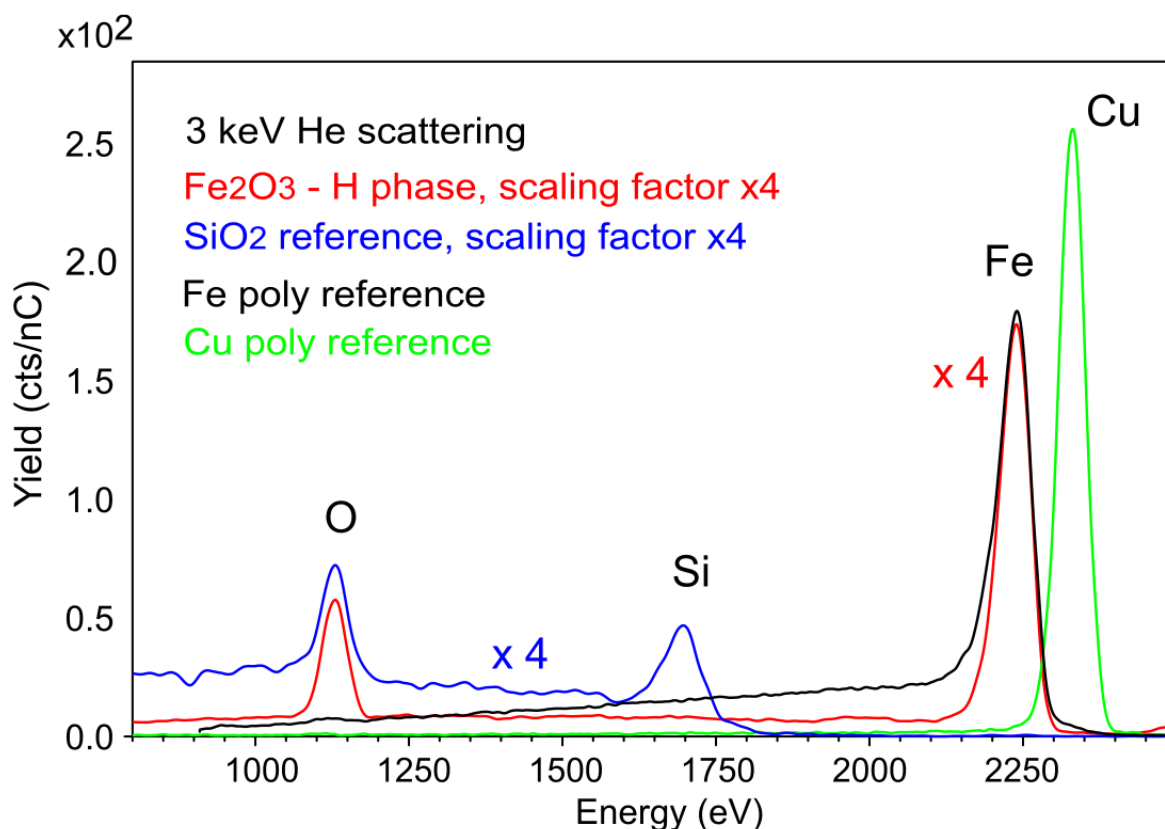


Fig.S2: LEIS spectra for helium (3.0 keV) scattering (145°) on the analyzed $\alpha\text{-Fe}_2\text{O}_3(0001)$ surface (H-phase) and on references (Fe, SiO_2 , and Cu). The spectra for SiO_2 and Fe_2O_3 were multiplied by a scaling factor of 4 for better visibility.

The instrumental factor c was evaluated from the helium scattering on a clean Cu polycrystalline surface within the range of primary energies from 1.0 keV to 2.2 keV. It is the AN mechanism which is dominant in this case, and thus the perpendicular inverse velocities were used in the calculation³.

The iron atomic surface concentration is evaluated using signals of relevant Fe peaks in Fig. S2 (primary energy 3.0 keV). Apparently, the charge exchange processes for the measured surface and Fe polycrystalline reference are dominated by CIN. The ratio is equal to 0.24 (please mind the scaling factor of 4 in Fig. S2). After the multiplication by the atomic surface concentration for the Fe reference $1.93 \times 10^{15} \text{ cm}^{-2}$ (calculated from the Fe density 7.87 g/cm^3) we obtain the value $0.46 \times 10^{15} \text{ cm}^{-2}$ for the H-phase.

Quantification of the O content is more demanding, because both neutralization mechanisms

are involved within the energy range used for our LEIS analysis; AN being dominant at lower energies and CIN at higher energies. These two energy ranges were distinguished for helium scattering on the SiO₂ surface by Téllez et al. ⁵. The CIN becomes dominant for primary energies above 3 keV.

Signal intensities divided by the instrumental factor and by the differential scattering cross-section are plotted in logarithmic scale against the sum of inverse velocities in Fig. S3. The ratio of intercepts of the fitted straight lines with the vertical axis (at infinite velocity) determines the ratio of O atomic surface densities in the analyzed surface and in the silica reference:

$$\frac{N_0^{Fe2O3}}{N_0^{SiO2}} = \frac{35.7}{34.7}$$

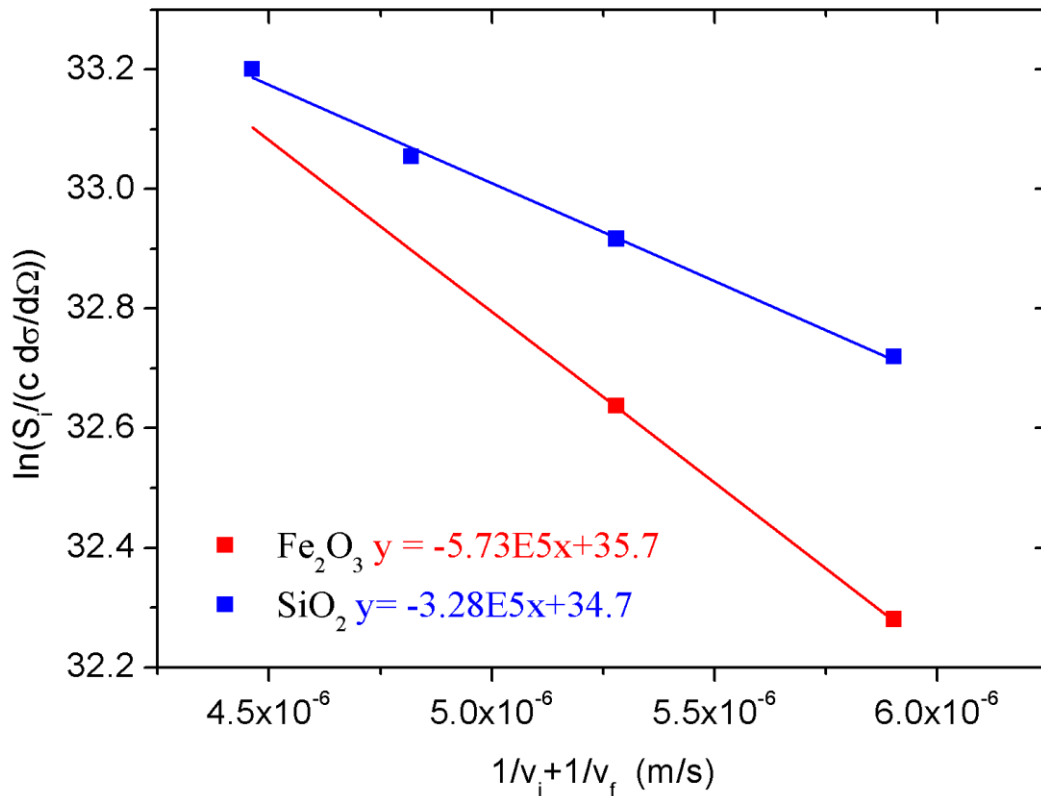


Fig.S3: Logarithmic plot of the O signal divided by the instrumental factor and by the scattering cross section for the analyzed surface (red) and for the silica reference (blue).

Taking into account the atomic surface concentration of O in the reference ($N_0^{SiO2} = 1.63 \times 10^{15}$ cm⁻² calculated from the SiO₂ density 2.32 g/cm³) we obtain the sought concentration $N_0^{Fe2O3} = 1.68 \times 10^{15}$ cm⁻² for the H-phase.

The calculated atomic surface concentration of O is 3.6 times higher than that of Fe atoms. It has to be mentioned that the O evaluation on H-phase is based on only two experimental

points (primary energies 4.0 keV and 5.0 keV) and thus the estimated relative uncertainty in the atomic surface concentration is about 30%. In summary, the LEIS analysis of the H-phase of the α -Fe₂O₃(0001) surface shows that oxygen atoms clearly predominate in the topmost atomic layer.

Nevertheless, the large difference of the atomic surface concentration of Fe and O in the Fe₂O₃ H-phase should be explained. The proposed 1T-FeO₂ model is terminated by an O atomic layer situated (after relaxation) about 0.9 Å above the plane with Fe atoms. This arrangement would exhibit dominant scattering of the O atoms over that of the Fe atoms.

The calculation based on screened Coulomb potential⁶ shows that the shadow cone radius for a 3.0-keV He projectile has at the distance of 0.9 Å behind the O atom a radius of only 0.27 Å. Thus, the shadow cones formed by O atoms at the incoming trajectory are not able to effectively screen the Fe atoms.

The situation is different with the outgoing trajectory, where the helium projectiles in specific azimuths pass relatively close to the upper O atoms (the Qtac 100 instrument collects scattered ions over the whole azimuth to increase the detection sensitivity). The resulting Fe signal is reduced by shielding due to neutralization at the vicinity of the O atoms. This mechanism was described and experimentally proved by van den Oetelaar et al.⁶ for He scattering on polycrystalline CuO. The Cu signal was reduced 5 times with respect to a signal estimated for Cu concentration calculated from the bulk density of CuO.

Theoretical calculations

The projector-augmented wave method, as implemented in the Vienna ab-initio simulation package (VASP) suite^{7,8}, was used for the calculations. The energy cutoff for the plane-wave expansion was set to 400 eV. For the exchange-correlation functional, we chose a semi-local generalized gradient approximation within the PBE parameterization⁹ in combination with effective Hubbard hamiltonian which described on-site Coulomb repulsion among d-electrons by an additional term U . Transition metal oxides are well known as strongly correlated materials due to repulsive electron-electron interaction between d-electrons and classical DFT functionals typically fail to describe such systems. We adopted simplified rotationally invariant approach to the GGA+ U introduced by Dudarev *et al.*^{9,10} and set $U_{\text{eff}} = U - J$ parameter to 5.3 eV^{11,12}. We used also hybrid screened exchange functional HSE06¹³ to test the results for free-standing FeO_2 . For the simulations of STM, we used a standard Tersoff-Hamann method, integrating the tunneling in the energy range -0.5 to 0.0 eV.

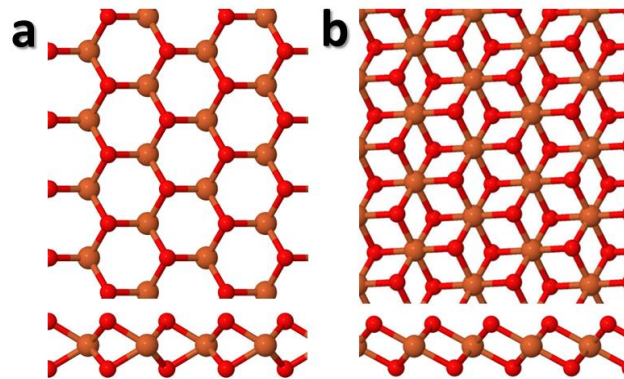


Fig.S4: The models of free-standing a) Hexagonal 2H form and b) trigonal 1T form of the FeO_2 layer.

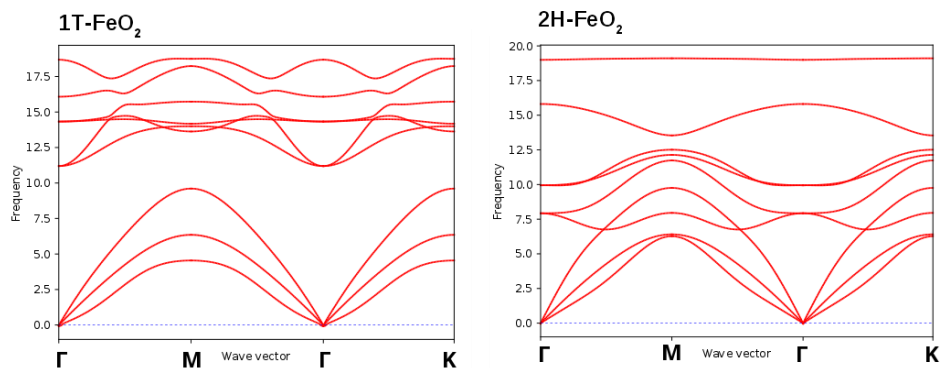


Fig.S5: Phonon dispersions (phonon frequency in THz) of free-standing single-layer of 1T- FeO_2 and 2H- FeO_2 calculated via density functional perturbation theory approach.

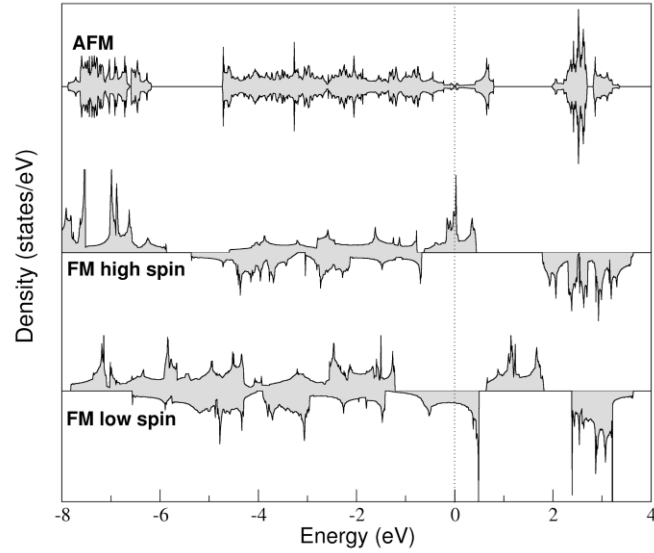


Fig.S6: The electronic density of states for the antiferromagnetic (AFM), high spin ferromagnetic (FM), and low spin FM phase of 1T-FeO₂. The Fermi level is aligned to zero of the energy.

Design of the full supercell models

For the calculation of the top lattice parameter (a_{top}), we use the known bulk hematite lattice constant $a_{\text{bulk}} = 5.038 \pm 0.002 \text{ \AA}$ ¹⁴, the superstructure lattice parameter $a_{\text{moiré}} = 40 \pm 1 \text{ \AA}$ measured by STM, and the relative superstructure orientation between domains $2\varphi = 8^\circ \pm 1^\circ$. Assuming that the superstructure arises from the interference of two lattices (a moiré), we have calculated the top layer lattice parameter $a_{\text{top}} = 3.14 \pm 0.01 \text{ \AA}$, and the lattice rotation with respect to the bulk lattice $30^\circ \pm \delta$ (for the two domains) with $\delta = 0.31^\circ \pm 0.04^\circ$. The top layer lattice parameter is within the range determined by the STM measurements ($3.08 \pm 0.08 \text{ \AA}$).

The obtained values describe a possibly incommensurate surface structure, and STM confirms that the superstructure is indeed incommensurate. For the purpose of the calculations, we have designed a commensurate model that best matches the measured parameters. The model is shown in Fig. S7, and it comprises $\begin{smallmatrix} 13 & 1 \\ -1 & 12 \end{smallmatrix}$ top-layer cells on $\begin{smallmatrix} 9 & 5 \\ -5 & 4 \end{smallmatrix}$ bulk cells or, in Wood's notation, a single-layer 1T-FeO₂-($\sqrt{157} \times \sqrt{157}$)R-4.0 on α -Fe₂O₃(0001)-($\sqrt{61} \times \sqrt{61}$)-R26.3 (for the $30^\circ + \delta$ domain). The parameters of this model are $a_{\text{moiré,model}} = 39.35 \text{ \AA}$, $a_{\text{top,model}} = 3.14 \text{ \AA}$, $\delta_{\text{model}} = 0.29^\circ$, and $2\varphi_{\text{model}} = 7.34^\circ$, in excellent agreement with the experimental values.

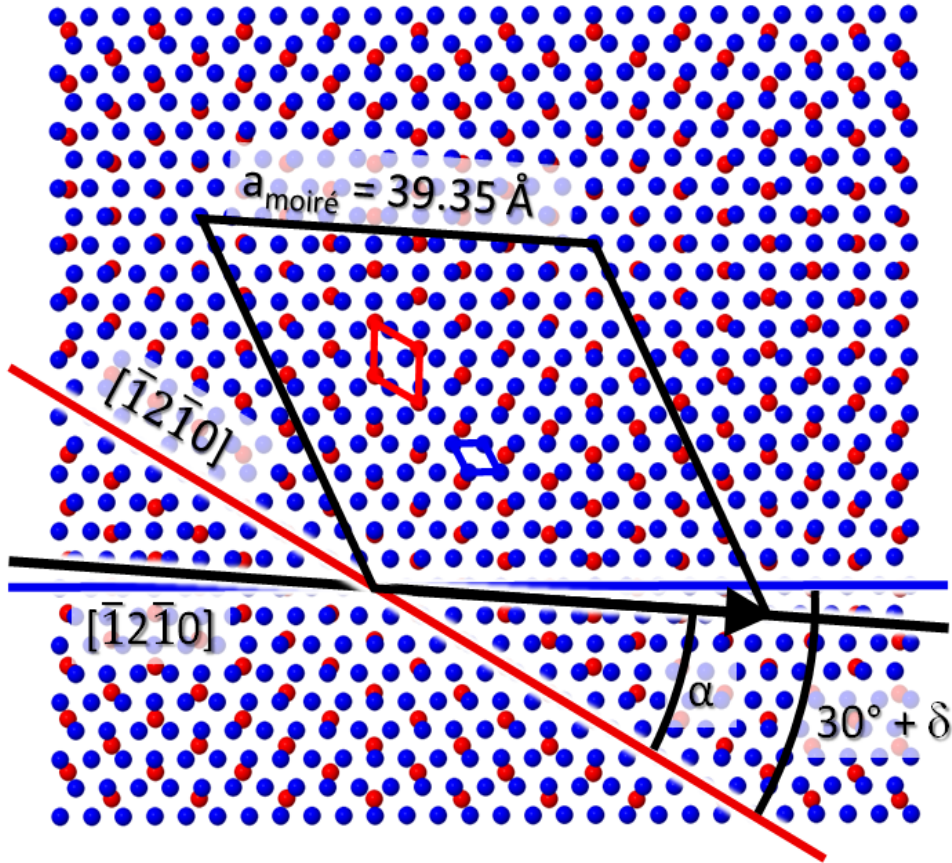


Fig. S7: One of the mirror-symmetrical variants of the best-matching Moiré model. Hexagonal grid representing the overlayer periodicity (3.14 Å blue dots) is placed on the top of a grid with the α -Fe₂O₃(0001) parameters (5.039 Å, red dots).

Stability of the models

Thermodynamic stability of various forms of an Fe oxide overlayer and hematite surface terminations can be assessed from the formation energy E_{form}

$$E_{form} = E_{tot} - n_{Fe} \mu_{Fe} - n_O \mu_O$$

where E_{tot} is the total energy of the system, μ_{Fe} the chemical potential of Fe, μ_O the chemical potential of O, and n_{Fe} , n_O the respective number of atoms. The temperature and pressure dependence of the formation energy was omitted as it makes negligible contribution at our experimental conditions. The Fe and O chemical potential are not independent, they are bound together by the existence of the hematite bulk phase. That allows to express E_{form} as a function of the O chemical potential

$$E_{form} = E_{tot} - \frac{1}{2} n_{Fe} \mu_{Fe_2O_3} - (3/2 n_{Fe} - n_O) \mu_O$$

The meaningful range of μ_{O} is limited by the conditions that the chemical potential of Fe has to be smaller than that of an atom of bulk Fe, and that the chemical potential of O has to be smaller than that of an O atom of O_2 molecule.

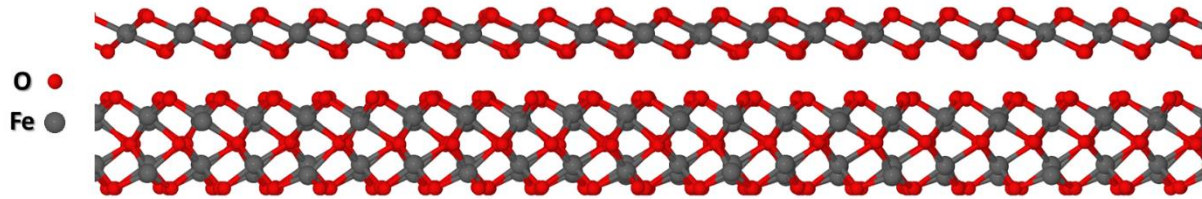


Fig. S8: Side-view of the ball-and-stick model of 1T- FeO_2 on O_3 -terminated $\alpha\text{-Fe}_2\text{O}_3(0001)$ bulk

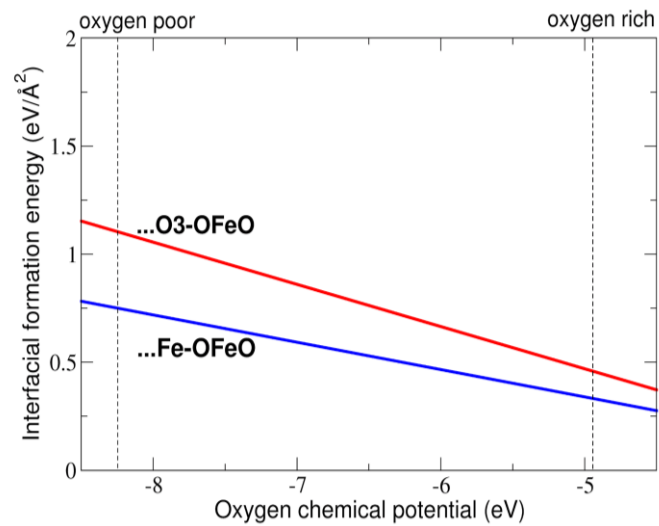


Fig. S9: Formation energies of the FeO_2 -hematite interface for two terminations of the bulk hematite, the half-metal (Fe) termination and the O_3 termination, as functions of the oxygen chemical potential, μ_{O} (O partial pressure). The physically possible range of μ_{O} is marked by vertical dashed lines).

References

1. Miller, D. J., Biesinger, M. C. & McIntyre, N. S. Interactions of CO₂ and CO at fractional atmosphere pressures with iron and iron oxide surfaces: one possible mechanism for surface contamination? *Surf. Interface Anal.* **33**, 299–305 (2002).
2. Genuzio, F., Sala, A., Schmidt, T., Menzel, D. & Freund, H.-J. Interconversion of α -Fe₂O₃ and Fe₃O₄ Thin Films: Mechanisms, Morphology, and Evidence for Unexpected Substrate Participation. *J. Phys. Chem. C* **118**, 29068–29076 (2014).
3. Brongersma, H., Draxler, M., Deridder, M. & Bauer, P. Surface composition analysis by low-energy ion scattering. *Surf. Sci. Rep.* **62**, 63–109 (2007).
4. Průša, S. *et al.* Highly Sensitive Detection of Surface and Intercalated Impurities in Graphene by LEIS. *Langmuir* **31**, 9628–9635 (2015).
5. Téllez, H. *et al.* Determination of ¹⁶O and ¹⁸O sensitivity factors and charge-exchange processes in low-energy ion scattering. *Appl. Phys. Lett.* **101**, 151602 (2012).
6. van den Oetelaar, L. C. A., van Benthem, H. E., J H J, Stapel, P. J. A. & Brongersma, H. H. Application of low-energy noble-gas ion scattering to the quantitative surface compositional analysis of binary alloys and metal oxides. *Surf. Interface Anal.* **26**, 537–548 (1998).
7. Blöchl, P. E. Projector augmented-wave method. *Phys. Rev. B: Condens. Matter Mater. Phys.* **50**, 17953–17979 (1994).
8. Kresse, G. & Joubert, D. From ultrasoft pseudopotentials to the projector augmented-wave method. *Phys. Rev. B: Condens. Matter Mater. Phys.* **59**, 1758–1775 (1999).
9. Perdew, J. P., Burke, K. & Ernzerhof, M. Generalized Gradient Approximation Made Simple. *Phys. Rev. Lett.* **77**, 3865–3868 (1996).
10. Dudarev, S. L., Botton, G. A., Savrasov, S. Y., Humphreys, C. J. & Sutton, A. P. Electron-energy-loss spectra and the structural stability of nickel oxide: An LSDA U study. *Phys. Rev. B: Condens. Matter Mater. Phys.* **57**, 1505–1509 (1998).
11. Wang, L., Maxisch, T. & Ceder, G. Oxidation energies of transition metal oxides within

- the GGA + U framework. *Phys. Rev. B: Condens. Matter Mater. Phys.* **73**, (2006).
12. Jain, A. *et al.* A high-throughput infrastructure for density functional theory calculations. *Comput. Mater. Sci.* **50**, 2295–2310 (2011).
 13. Heyd, J., Scuseria, G. E. & Ernzerhof, M. Erratum. Hybrid functionals based on a screened Coulomb potential. *J. Chem. Phys.* **124**, 219906 (2006).
 14. Blake, R. L. & United States. Bureau of Mines. *Refinement of hematite crystal structure.* (1970).